

PIC simulations of stable surface waves on a subcritical fast magnetosonic shock front

M. E. Dieckmann

Dept. of Science and Technology (ITN), Linköping University, Campus Norrköping, SE-60174 Norrköping, Sweden

E-mail: mark.e.dieckmann@liu.se

C. Huete

Univ Carlos III Madrid, Grp Mekan Fluidos, Leganes 28911, Spain

F. Cobos

Univ Castilla La Mancha, ETSI Ind, Ciudad Real 13071, Spain

A. Bret

Univ Castilla La Mancha, ETSI Ind, Ciudad Real 13071, Spain

D. Folini

Univ Lyon, ENS de Lyon, Univ Lyon 1, CNRS, Centre de Recherche Astrophysique de Lyon UMR5574 F-69230, Saint-Genis-Laval, France

B. Eliasson

Univ Strathclyde, SUPA, Glasgow G4 0NG, Scotland, UK

R. Walder

Univ Lyon, ENS de Lyon, Univ Lyon 1, CNRS, Centre de Recherche Astrophysique de Lyon UMR5574 F-69230, Saint-Genis-Laval, France

August 2022

Abstract. We study with particle-in-cell (PIC) simulations the stability of fast magnetosonic shocks. They expand across a collisionless plasma and an orthogonal magnetic field that is aligned with one of the directions resolved by the 2D simulations. The shock speed is 1.6 times the fast magnetosonic speed when it enters a layer with a reduced density of mobile ions, which decreases the shock speed by up to 15% in 1D simulations. In the 2D simulations, the density of mobile ions in the layer varies sinusoidally perpendicularly to the shock normal. We resolve one sine period. This variation only leads to small changes in the shock speed evidencing a restoring force that opposes a shock deformation. As the shock propagates through the layer, the ion density becomes increasingly spatially modulated along the shock front and the

magnetic field bulges out where the mobile ion density is lowest. The perturbed shock eventually reaches a steady state. Once it leaves the layer, the perturbations of the ion density and magnetic field oscillate along its front at a frequency close to the lower-hybrid frequency; the shock is mediated by a standing wave composed of obliquely propagating lower-hybrid waves. We perform three 2D simulations with different box lengths along the shock front. The shock front oscillations are aperiodically damped in the smallest box with the fastest variation of the ion density, strongly damped in the intermediate one, and weakly damped in the largest box. The shock front oscillations perturb the magnetic field in a spatial interval that extends by several electron skin depths upstream and downstream of the shock front and could give rise to Whistler waves that propagate along the shock's magnetic field overshoot. Similar waves were observed in hybrid and PIC simulations and by the MMS satellite mission.

Keywords: fast magnetosonic shock, PIC simulations, shock boundary oscillations

This is a peer reviewed, accepted author manuscript of the following research article: Dieckmann, M. E., Huete, C., Cobos, F., Bret, A., Folini, D., Eliasson, B., & Walder, R. (2023). PIC simulations of stable surface waves on a subcritical fast magnetosonic shock front. *Physica Scripta*. <https://doi.org/10.1088/1402-4896/ace801>

1. Introduction

Shocks in collisionless plasma, in which effects due to Coulomb collisions between charged particles are negligible compared to collective electromagnetic forces, have been studied in the laboratory [1, 2, 3, 4, 5], in the Solar system [6], and by means of numerical simulations [7, 8, 9, 10, 11, 12, 13, 14, 15, 16, 17, 18, 19, 20, 21]. Shocks are important structures for the dissipation of energy in collisionless plasma (See [16] for a recent review). We consider here perpendicular nonrelativistic fast magnetosonic (FMS) shocks, for which the magnetic field upstream of the shock is oriented orthogonally to its normal and is amplified by the shock crossing. In the reference frame of the shock, the plasma is slowed down, heated, and compressed by the shock crossing.

Fast magnetosonic shocks are categorized according to how the shock speed in the upstream frame of reference compares to the speed of the magnetohydrodynamic FMS wave. If the shock speed is less than 2.7 times the FMS speed [22], the shock is subcritical and its electric cross-shock potential can slow down the plasma to a speed below the FMS speed. Another estimate [23] sets this number to a value below 2.7. If the shock is faster, the particle distributions around the shock become nonthermal [24]. Such distributions, which can involve for example particle beams or an anisotropic temperature, give rise to instabilities that modify or destroy the shock. Perpendicular subcritical shocks are stationary in time in their rest frame and they have a thin transition layer, which enables accurate measurements of their position.

The Magnetospheric Multiscale Spacecraft (MMS) mission detected ripples on the surface of the Earth's bow shock [6]. Surface waves on plasma boundaries [25, 26, 27] can be stimulated by perturbations. Perturbations develop out of drift instabilities [20, 28, 29, 30] if plasma flows along a stationary boundary like a tangential discontinuity. Perturbations can also grow near shock surfaces. Shock-reflected ions can move far upstream of the shock and drive waves [11, 31] letting shocks propagate into an upstream medium with a spatially nonuniform density and magnetic field direction. Lowe and Burgess [9] found boundary waves on the shock in their two-dimensional hybrid simulation, which used a kinetic approximation for ions and described electrons with an inertialess fluid. These waves were distributed over a wide wavenumber interval and followed the dispersion relation of the Alfvén wave [32]. Burgess and his coworkers extended the simulation domain to three dimensions and examined the interplay of the ripples with ion-driven instabilities and the therefrom resulting waves [15].

Hybrid codes approximate electrons by an inertialess fluid. Resolving their full dynamics is more expensive but it allows particle-in-cell (PIC) simulations to model high-frequency processes, where electron dynamics matters. Several PIC simulation studies have addressed the interplay of subcritical [21] and supercritical collisionless shocks [8, 12, 17] with the shock-modified upstream plasma. These studies covered a wide range of magnetic field strengths and orientations relative to the shock normal. Alfvénic shock ripples accelerated electrons and led to the growth of high-frequency waves like Whistlers. The plasma was not fully thermalized after its passage through

the shock and relaxed through secondary instabilities. On ion gyro-scales, the shock was immersed in a transition layer where many waves and plasma structures were coupled across different spatial and temporal scales.

The aforementioned simulations and the pioneering hybrid simulation in Ref. [7] suggest that stable, oscillatory shock surface modes exist in collisionless plasma that can be excited by perturbations of the upstream plasma and travel along the shock surface. In this context, the term stable means that once these surface waves have been excited, their amplitude remains constant or decreases.

The fundamental requirement for the existence of a stable surface wave is the presence of a restoring force, which serves to counteract the effects of perturbations. In the context of gas dynamics shocks, the mode is an acoustic one and the restoring force is provided by a combination of tangential velocity conservation and the unbalanced pressure field, leading to the formation of oscillating shock ripple patterns. For an ideal gas, the amplitude of these oscillations decreases over time proportional to $t^{-3/2}$, or $t^{-1/2}$ in the strong-shock limit, as demonstrated by the works of Roberts [33], Freeman [34], and Zaidel [35]. The stability limits, beyond which the shock perturbation may experience non-decaying behavior or even exponential growth, have been extensively studied and documented, departing from the pioneering works of D'yakov [36] and Kontorovich [37] and continuing to high-energy-density conditions [38, 39]. The extension of these results to magnetohydrodynamics may not be trivial since additional magnetic restoring forces may appear. The first work on the stability limits of FMS shock in ideal conditions, characterized by an ideal gas equation of state and a perfectly conducting gas, was performed by Gardner [42]. However, further research is necessary to fully understand the transient evolution of these perturbations. If FMS shock perturbations are damped and the damping rate is lower than their oscillation frequency, they have the potential to generate surface waves, as has been observed at the Earth's bow shock and in PIC and hybrid simulations.

In the previous hybrid- and PIC simulations, the upstream perturbations were driven primarily by the shock-reflected ion beam. In such a setting, the driver of the shock boundary oscillations cannot be separated from the shock boundary, which is characterized by an overshoot of the magnetic amplitude and density over its values downstream of the shock. This separation is necessary if we want to compare the oscillations of the shock boundary to shock modes in (magneto-)hydrodynamic models, which are usually taken to be monochromatic in wavenumber space. We can decouple the driver from the shock boundary by perturbing it once and letting it relax.

We study the evolution of a perturbation of the shock front with one- and two-dimensional particle-in-cell (PIC) simulations. We align the uniform magnetic field of the upstream plasma with the direction of the 2D simulation that is perpendicular to the shock normal. The magnetic field direction is unresolved in the 1D simulations. A thermal pressure gradient drives an initially planar subcritical FMS shock. We follow it through a spatially uniform magnetized ambient plasma with a ratio between the electron thermal pressure and the magnetic pressure ≈ 0.55 . The shock propagates

across a perturbation layer with a limited extent along the shock propagation direction. The number density of mobile electrons in this layer equals that of the surrounding plasma. The positive charge density in the perturbation layer is subdivided into two components. The number density of mobile ions is constant along the shock propagation direction and is equal to or less than that of the surrounding ambient plasma. An immobile positive charge cloud cancels out the negative net charge. In the perturbation layer of the 2D simulations, the number density of the mobile ions varies in the direction perpendicular to the shock normal. By selecting a sinusoidally varying perturbation, we isolate a single surface mode. We obtain the following results.

Shocks in the 1D simulations propagate at a lower speed through the perturbation layer and regain their initial speed after they leave it. Based on this finding and the structure of the perturbation layer in the 2D simulations, the position of the shock front in the direction of the average shock normal should vary sinusoidally along the front and its amplitude should grow with time for as long as the shock moves through the perturbation layer. The amplitude does, however, saturate after an initial growth phase and remains constant after that. The density at the shock overshoot and the magnetic field direction also become functions of the position along the shock front. Once the shock leaves the perturbation interval and enters the spatially uniform upstream plasma, the spatial, density- and magnetic field perturbations perform oscillations around their equilibrium values. Their oscillation frequency is just below the lower-hybrid frequency and involve also the shock mode, which separates the upstream from the downstream plasma. The shock mode and the surface wave thus form an oblique FMS mode near its resonance frequency where it becomes quasi-electrostatic.

Our paper is structured as follows. Section 2 summarizes the numerical scheme used by the PIC code, the initial conditions of our simulations, the FMS mode and its coupling to lower-hybrid waves, and results from 1D simulations. Section 3 presents results from 2D simulations and Section 4 discusses our findings and their implications.

2. The simulation code and its initial conditions

2.1. The simulation code EPOCH

PIC codes approximate each plasma species i by resolving its velocity distribution function with a cloud of computational particles (CPs). Each CP j of species i is characterized by a charge Q_j and mass M_j with a value Q_j/M_j , which matches the charge-to-mass ratio Q_i/M_i of a particle of species i . Every CP has a position \mathbf{x}_j and velocity \mathbf{v}_j and, hence, a spatially localized current density $\propto Q_j \mathbf{v}_j$. The summation of the current density contributions of all CPs yields the macroscopic current density $\mathbf{J}(\mathbf{x}, t)$. The electric field $\mathbf{E}(\mathbf{x}, t)$, magnetic field $\mathbf{B}(\mathbf{x}, t)$ and current density $\mathbf{J}(\mathbf{x}, t)$ are defined on a numerical grid and the latter updates $\mathbf{E}(\mathbf{x}, t)$ and $\mathbf{B}(\mathbf{x}, t)$ according to discretized forms of Ampère's law

$$\nabla \times \mathbf{B} - \frac{1}{c^2} \frac{\partial \mathbf{E}}{\partial t} = \mu_0 \mathbf{J}, \quad (1)$$

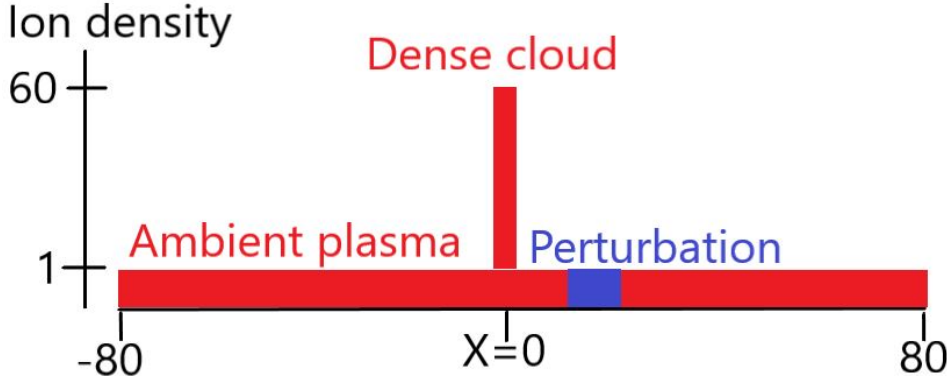


Figure 1. The ion density distribution at the time $t = 0$ in units of n_{i0} : The ambient plasma has the density 1. A dense cloud in the interval $-3 \leq x \leq 3$ has a density 60. The density of mobile ions in the perturbation layer $8.9 \leq x \leq 20.8$ is constant along x but varies along y in the 2D simulations. Its value varies between 0.4 and 1.0. In the 2D simulations, the initial ion density distribution does not change with y outside of the perturbation layer.

where μ_0, c are the vacuum permeability and speed of light, and Faraday's law

$$\nabla \times \mathbf{E} + \frac{\partial \mathbf{B}}{\partial t} = 0. \quad (2)$$

The EPOCH code fulfills $\nabla \cdot \mathbf{B} = 0$ and Gauss' law $\nabla \cdot \mathbf{E} = \rho/\epsilon_0$ (ρ, ϵ_0 : charge density and vacuum electric permittivity) to round-off precision [40]. Once the electromagnetic fields have been updated, they are interpolated to the position of each CP and update its momentum according to the relativistic Lorentz equation. All particle velocity components and, hence, all components of \mathbf{E} , \mathbf{B} , and \mathbf{J} are updated also in simulations that resolve fewer than 3 spatial dimensions. This computational cycle is repeated for as many time steps Δ_t as necessary to cover the time scale of interest. More details of the numerical scheme of the EPOCH code are given elsewhere [41].

2.2. Initial conditions

All simulations cover the interval $-L_x/2 \leq x \leq L_x/2$. The 2D simulations also resolve an interval $0 \leq y \leq L_y$. Values of L_x and L_y vary between simulations. Boundary conditions are periodic in all directions. We model fully ionized nitrogen at the correct ion-to-electron mass ratio because it is widely used in laser-plasma experiments, for example in Ref. [3]. Figure 1 sketches the initial number density distribution of the ions along x . In the ambient plasma, we set the electron number density to n_{e0} and that of the ions to $n_{i0} = n_{e0}/7$. The electron plasma frequency $\omega_{pe} = (n_{e0}e^2/\epsilon_0 m_e)^{1/2}$ (e, m_e, c : elementary charge, electron mass, and light speed) sets the electron skin depth $\lambda_e = c/\omega_{pe}$, with which we normalize space. At the time $t = 0$, the electric and magnetic fields are set to $\mathbf{E} = (0, 0, 0)$ and $\mathbf{B} = (0, B_0, 0)$ with $eB_0/m_e\omega_{pe} = 0.084$. All ions have a temperature 200 eV. Electrons outside (inside) the dense cloud have a temperature 1000 eV (1500 eV). Thermal diffusion lets more electrons stream from the dense into the

Electron gyrofrequency $\omega_{ce} = eB_0/m_e\omega_{pe}$	0.084	$\omega_{ce}t_{sim} = 1200$
Ion gyrofrequency $\omega_{ci} = 7eB_0/m_i\omega_{pe}$	2.3×10^{-5}	$\omega_{ci}t_{sim} = 0.33$
Ion plasma frequency $\omega_{pi} = (49e^2n_{i0}/\epsilon_0m_i)^{1/2}/\omega_{pe}$	0.0165	$\omega_{pi}t_{sim} = 240$
Lower-hybrid frequency $\omega_{lh} = ((\omega_{ce}\omega_{ci})^{-1} + \omega_{pi}^{-1})^{-1/2}/\omega_{pe}$	0.0014	$\omega_{lh}t_{sim} = 20$
Electron thermal speed $v_{te} = (k_B T_e/m_e)^{1/2}/c$	0.044	$v_{te}t_{sim}/\lambda_e = 640$
Ion-acoustic speed $c_s = (k_B(7\gamma_e T_e + \gamma_i T_i)/m_i c^2)^{1/2}$	9.4×10^{-4}	$c_s t_{sim}/\lambda_e = 13.7$
Alfvén speed $v_A = B_0/(\mu_0 c^2 n_{i0} m_i)^{1/2}$	1.4×10^{-3}	$v_A t_{sim}/\lambda_e = 20.0$
FMS speed $v_{fms} = (c_s^2 + v_A^2)^{1/2}/c$	1.7×10^{-3}	$v_{fms} t_{sim}/\lambda_e = 24.3$
Electron thermal gyroradius $v_{te}/\omega_{ce}\lambda_e$	0.53	
Electron Debye length $v_{te}/\omega_{pe}\lambda_e$	0.044	

Table 1. The relevant normalized frequencies, speeds, and spatial scales for the physical values $n_{e0} = 10^{21} \text{m}^{-3}$ and $B_0 = 0.85 \text{ T}$ we used in our simulation setup and for $t_{sim} = 14500$ (in units of ω_{pe}^{-1}).

ambient plasma than in the opposite direction, which yields an ambipolar electric field that points from the dense to the diluted plasma. This electric field lets the ions of the dense plasma expand into the ambient plasma. It also accelerates ambient electrons into the dense cloud. The accelerated ambient electrons form a beam that interacts with the electrons of the dense cloud. We give the latter a higher temperature in order to reduce the effects of a two-stream instability between both electron populations.

The temperature $T_e = 1000 \text{ eV}$ of the electrons in the ambient plasma sets their thermal speed $v_{te} = (k_B T_e/m_e)^{1/2}$ (k_B : Boltzmann constant). The ion temperature $T_i = 200 \text{ eV}$ and T_e set the ion acoustic speed c_s in the ambient plasma. On the time scales of ion-acoustic oscillations, electrons have three degrees of freedom and ions have one. This gives the adiabatic constants $\gamma_e = 5/3$ for electrons and $\gamma_i = 3$ for ions. The ion-acoustic speed becomes $c_s = (k_B(7\gamma_e T_e + \gamma_i T_i)/m_i)^{1/2}$. The Alfvén speed $v_A = B_0/(\mu_0 n_{i0} m_i)^{1/2}$ and c_s define the FMS speed $v_{fms} = (c_s^2 + v_A^2)^{1/2}$. Our plasma has the electron plasma beta $\beta = n_{e0} k_B T_e / (B_0^2 / 2\mu_0) = 0.55$. Relevant plasma parameters in the uniform ambient plasma and their values are listed in Table 1. Although we selected parameters in our simulation setup, which are representative of some laser-plasma experiments where physical scales matter, we use normalized units scaled to the electron skin depth λ_e , the electron plasma frequency ω_{pe} , and the speed of light c .

We consider here FMS shocks that propagate through the ambient plasma. Wave dispersive properties of FMS shocks are set by the plasma conditions in the downstream plasma. However, the density and magnetic field amplitude do not vary much between the upstream (ambient) plasma and downstream plasma of a subcritical FMS shock. We discuss wave properties in the ambient plasma and assume that they are also representative of the downstream plasma.

The FMS mode is not dispersive for low wavenumbers k . Since shocks form by a steepening of the wavefront, the wavenumbers of the waves that form the shock increase in time. Eventually, they reach values where the FMS mode becomes dispersive.

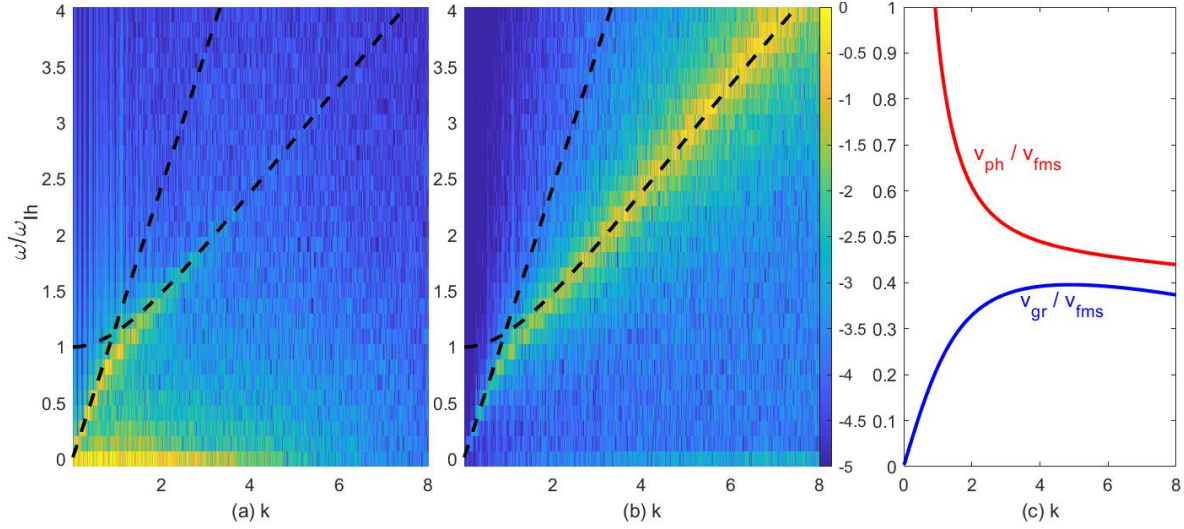


Figure 2. Wave spectrum in the ambient plasma as a function of the wavenumber k (normalized to λ_e) and the frequency ω , which we normalize here to ω_{lh} : Panel (a) shows the power spectrum of the noise in the B_y component and panel (b) that of the E_x component. The power spectra are normalized to their peak value and displayed on the same 10-logarithmic color scale. The dashed lines show the FMS mode $\omega_{EM}(k)$ and the lower-hybrid mode $\omega_{ES}(k)$. Panel (c) plots the phase velocity v_{ph} (red) and group velocity v_{gr} (blue) computed from $\omega_{ES}(k)$.

Simplified expressions for the dispersion relation of FMS waves in collisionless plasma can be obtained by either neglecting space charge, which gives $\omega_{EM}(k) = v_{fms}k$, or by taking the electrostatic limit where the electric field is tied to oscillations of the charge density. The latter gives the lower-hybrid mode $\omega_{ES}(k) = (3v_{ti}^2k^2 + \omega_{pi}^2(\omega_{ce}^2 + v_{te}^2k^2)/(\omega_{pe}^2 + \omega_{ce}^2 + v_{te}^2k^2))^{1/2}$ with the ion thermal speed $v_{ti} = (k_B T_i / m_i)^{1/2}$.

We use the noise distribution of the PIC code to track the full wave branch and show how it goes over into limits $\omega_{EM}(k)$ and $\omega_{ES}(k)$. Charge- and current-density fluctuations due to the moving CPs yield electric and magnetic field fluctuations. These fluctuations will have values of k and ω , which are connected to the particle motion. If CPs create fluctuations with such values of k, ω , they can often also absorb them. Hence, strong fluctuations of the electric and magnetic fields tend to reveal locations in k, ω -space where waves resonate with particles. They are strongest close to eigenmodes of the plasma (See [45] for a related discussion). The FMS mode compresses the background magnetic field and we can use fluctuations of B_y to track FMS modes in k, ω -space. In our 1D geometry, fluctuations in E_x are always tied to electrostatic charge density fluctuations and we use E_x to identify the lower-hybrid mode in k, ω -space.

Figure 2 shows the power spectra of the fluctuations in the magnetic B_y and electric E_x components. We computed them by running a 1D PIC simulation that resolved x with the plasma parameters of the ambient plasma discussed above. We Fourier-transformed $B_y(x, t)$ and $E_x(x, t)$ over space and time and multiplied the result with its complex conjugate giving $|B_y(k, \omega)|^2$ and $|E_x(k, \omega)|^2$. The noise at low wavenumbers k

is magnetic and follows ω_{EM} . At large k , the electric field noise maps out lower-hybrid waves. The waves that connect ω_{EM} with ω_{ES} at $k \approx 1$ have significant electric and magnetic components. They are thus not represented correctly by either limit.

Shocks form in our simulations just before the expanding ions reach the perturbation layer. We change the number density of mobile ions in this interval in Fig. 1 and keep that of mobile electrons unchanged. Since we set $\mathbf{E} = 0$ at $t = 0$, Gauss' law $\nabla \cdot \mathbf{E} = \rho/\epsilon_0$ implies initially a zero total plasma charge density $\rho = 0$ everywhere, which places an immobile positive charge density in our perturbation layer. Its electric field cancels out the one caused by the jump in the number density of mobile ions.

The 1D simulations and the 2D simulations 1 and 2 resolve $L_x = 160$ with 8000 grid cells and end at the time $t_{sim} = 14500$. The 2D simulation 3 uses 9000 grid cells to resolve $L_{x,3} = 180$ and follows the shock for the time $t_{sim,3} = 1.25t_{sim}$. The 2D simulations 1-3 resolve $L_{y,1} = 12$ by 600 cells, $L_{y,2} = 24$ by 1200 cells, and $L_{y,3} = 36$ by 1800 cells. The data is averaged over 4 cells in the 1D simulations and over patches of 2×2 cells in the 2D simulations. In the 2D (1D) simulations, ions and electrons are resolved by 25 CPs (375 CPs) per cell each.

2.3. One-dimensional simulations

We test with two 1D simulations how shocks react to changes in the number density of mobile ions in the perturbation layer. One 1D simulation represents $0.7n_{i0}$ by mobile ions and the other 1D simulation represents $0.4n_{i0}$ by mobile ions. According to Fig. 1, one shock will be launched at the density jump to the right of the dense cloud and a second one at the density jump to its left. Both will propagate away from the dense cloud and into the ambient plasma. Only the shock that moves to the right propagates through the perturbation layer. The left-moving shock in one of the simulations is taken as the reference shock. We invert the sign of the position x and velocity v_x in our plots so that we can compare the ion phase space density distribution of the left-moving unperturbed shock with that of the right-moving perturbed shock.

Figure 3 shows ion phase space density distributions. The supplementary movie 1 animates their evolution in time until $t_{sim} = 14500$. At $t_1 = 2000$, a localized oscillation of the ion phase space density distribution is growing at $x \approx 8$. We may interpret it as a steepening wave. It breaks shortly after this time and changes into a shock [19]. The magnetic field of the shock traps the electrons ahead of it and pushes them upstream. The current of the moving electrons and their space charge induces an electric field. It accelerates the practically unmagnetized ions with $\omega_{ci}t_{sim} \ll 2\pi$ ahead of the shock until their current balances the electronic one, giving rise to the shock foot. The change in the ion number density near the boundary $x = 8.9$ of the perturbation layer in Figs. 3(b, c) is compensated by a faster motion of the ions in the perturbed interval.

At $t_2 = 5000$ or $\omega_{ih}t_2 = 2.2\pi$, qualitative differences can be observed between the three shocks. Most downstream ions in the interval $12 \leq x \leq 16$ in Fig. 3(d) move at a speed below v_{fms} while the mean speed of those in Fig. 3(e) is about v_{fms} . The

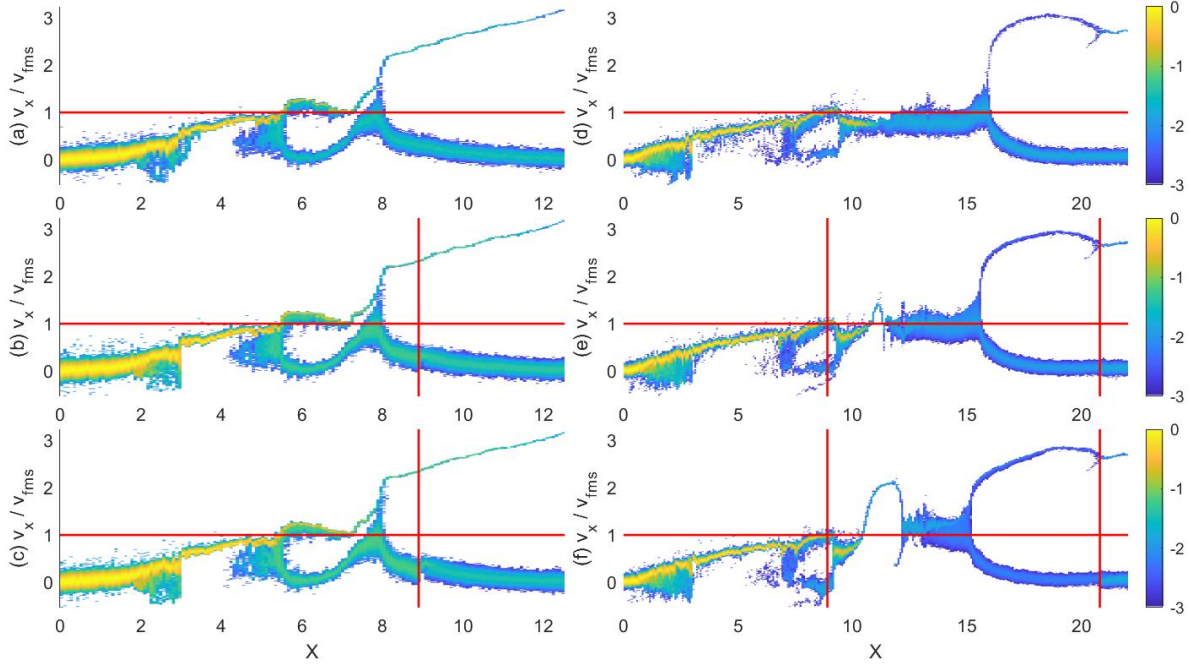


Figure 3. Ion phase space density distributions at the time $t_1 = 2000$ (left column) and $t_2 = 5000$ (right column). Panels (a, d) correspond to the simulation with the unperturbed plasma. Panels (b, e) show the distributions for the simulation with a mobile ion density $0.7n_{i0}$ in the interval $8.9 \leq x \leq 20.8$. Panels (c, f) show the distributions for the simulation with a mobile ion density $0.4n_{i0}$ in the interval $8.9 \leq x \leq 20.8$. All distributions are normalized to the peak value at $t = 0$ and shown on the same 10-logarithmic color scale. The vertical red lines indicate the boundaries of the perturbed interval while the horizontal ones plot the FMS speed.

downstream ions in Fig. 3(f) are confined to a smaller interval $13 \leq x \leq 15$ and most ions move faster than v_{fms} . Despite its faster downstream ions, the shock at $x = 15$ in Fig. 3(f) is trailing those in Figs. 3(d, e). Fewer ions, which cross the shock, reduce the thermal pressure behind it and, hence, the shock speed in the downstream frame. Figure 3(f) also shows that the slowdown of the perturbed shock decreased the speed of the reflected ions. The ions at $x \approx 20$, which were reflected by the shock when it just entered the perturbation layer, have a speed $\approx 3v_{fms}$. Those at $x \approx 17$, which were reflected after the slowdown of the shock, reach a speed of only $2.2v_{fms}$.

In Fig. 3(d), the mean velocity of the ions is approximately constant for $9.5 \leq x \leq 16$. The ion density change at $x \approx 11$ is caused by a tangential discontinuity, which balances the high thermal pressure of the blast shell plasma against the combined thermal and magnetic pressure of the shocked ambient plasma. As the shocks in Figs. 3(e, f) move into the perturbed interval, the pressure ahead of the tangential discontinuity decreases. Blast shell ions accelerate for $10 \leq x \leq 11$ in Figs. 3(e, f) in the ambipolar electric field of the blast shell's density gradient and decelerate at larger x , transferring their momentum to the downstream plasma.

Figures 3(d, e, f) show a structure in the shock-reflected ion beam at $x \approx 21$ and $v_x/v_{fms} \approx 2.8$. It develops when the shock-reflected ion beam, which has not yet

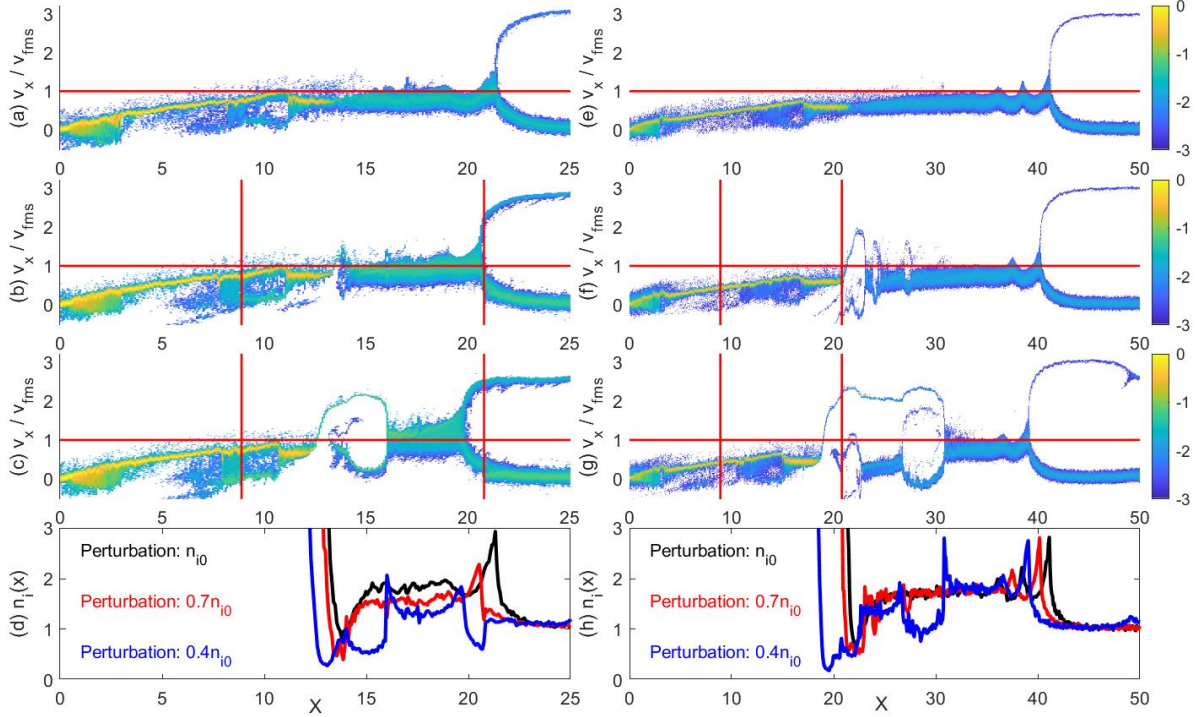


Figure 4. Ion density and phase space density distributions at the time $t_3 = 7000$ (left column) and $t_{sim} = 14500$ (right column). Panels (a, e) correspond to the simulation with the unperturbed plasma. Panels (b, f) show the distributions for the simulation with a mobile ion density $0.7n_{i0}$ in the interval $8.9 \leq x \leq 20.8$. Panels (c, g) show the distributions for the simulation with a mobile ion density $0.4n_{i0}$ in the interval $8.9 \leq x \leq 20.8$. All distributions are normalized to the peak value at $t = 0$ and shown on the same 10-logarithmic color scale. Panels (d, h) plot the densities of the mobile ions at the times t_3 and t_{sim} , respectively.

developed at the snapshots for $t_1 = 2000$, catches up with the ions at the front of the rarefaction wave that is visible in Figs. 3(a, b, c) at high speeds for $x > 8$ (See supplementary movie 1).

Figure 4 shows the ion phase space density distributions at later times. We also plot the distributions of the ion densities that correspond to those of the phase space density. At $t_3 = 7000$ ($\omega_{lh}t_3 = 3.1\pi$), the shocks are about to leave the perturbation layer. As before, the mean velocity of the downstream ions increases, and the shock speed in their rest frame decreases with a decreasing number density of the mobile ions ahead of the shock. A substantial lag is observed in particular for the shock in Fig. 4(c). The ion densities for this time are plotted in Fig. 4(d). In the overshoot of the unperturbed shock, the ion density reaches the value 3. It decreases to just below 2 downstream of the shock. The shocks, which move through the perturbation layer, have a lower density of their downstream plasma, and the ion density at their overshoot reaches about 3 times that of the mobile ions in the perturbation layer. At $t_{sim} = 14500$ ($\omega_{lh}t_{sim} = 6.4\pi$), the shock speed and the mean velocity of the downstream ions behind the shocks are similar. The ion phase space vortices [44] in Fig. 4(f, g) have been separated from the

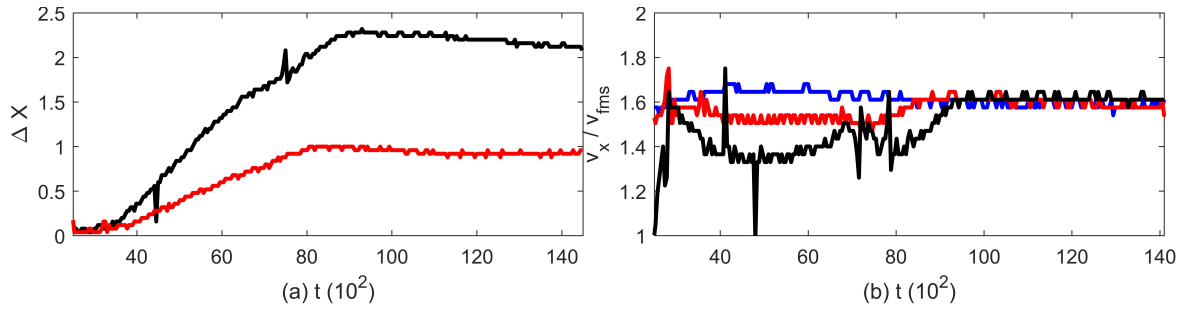


Figure 5. Time evolution of the shock separation and speed: Panel (a) plots the separation of the unperturbed shock and the one that propagated through the ion perturbation with the density $0.7n_{i0}$ (red curve). The black curve shows the lag of the shock that propagated through the ion perturbation with the density $0.4n_{i0}$. Panel (b) plots the speed of the shock that propagates through the unperturbed plasma (blue), through the one with $0.7n_{i0}$ mobile ions (red), and with $0.4n_{i0}$ (black).

shock by the influx of shocked upstream plasma. The density distributions near the overshoots in Fig. 4(h) are similar for all shocks apart from a displacement along x .

Figure 5 quantifies the impact of the changed density of mobile ions on the shock speed and position. We identify the position, where the shock is located, as the one with the largest curvature of the ion density and track it over time. We averaged the ion density over several grid cells to decrease statistical fluctuations of the ion density, which reduces the accuracy with which we can determine the spatial position of the shock's overshoot. The method, with which we determined the shock position, does also not always find the exact position of the shock in particular in the perturbation layer with the density of mobile ions $0.4n_{i0}$, which created several outliers in the data. Inaccuracies will be visible in particular in the velocity data that is obtained by differentiating the noisy position data. Nevertheless, the computed curves reveal trends that are confirmed by the supplementary movie 1. Figure 5(a) plots the separation of the reference shock, which moves through the unperturbed plasma, from the two shocks that move through the perturbed plasma. We start plotting the separation after $t = 2500$ when the shock fully reformed in Figs. 3(a-c). The shock moving through the perturbation layer with the mobile ion density $0.7n_{i0}$ falls steadily behind the unperturbed shock until $t \approx 8000$ when Fig. 4(b) shows that it crosses the upper boundary $x = 20.8$ of the perturbed interval. The shock, which moves through the plasma with the mobile ion density $0.4n_{i0}$, leaves the perturbation layer last. Hence it is slowed down until $t \approx 10^4$. Figure 5(b) obtains the shock speed from the change of its position over a time interval ≈ 640 . The speeds of the shocks remain above $1.3v_{fms}$ for all times. Given that the FMS wave with frequencies just below ω_{lh} is dispersive and that its phase speed is well below v_{fms} at wave numbers $k \approx 1$ in Fig. 2, the Mach numbers are higher.

3. Two-dimensional simulations

3.1. A comparison of the boundary oscillations in the 2D simulations

In what follows, the term "simulation j " with $1 \leq j \leq 3$ refers to the 2D simulation with the length $L_{y,j}$ along y . We express the number density of mobile ions $n_i(x, y)$ in units of n_{i0} and the in-plane magnetic field is $B(x, y) = (B_x^2 + B_y^2)^{1/2}/B_0$. The magnetic B_z component remains at noise levels. The perturbation layer covers again $8.9 \leq x \leq 20.8$. Within the perturbation layer of simulation j , the density of mobile ions varies as $n_i(x, y) = 0.7 + 0.3 \sin(2\pi y/L_{y,j})$ for $0 \leq y \leq L_{y,j}$. We take the shock that moves in the direction of decreasing $x < 0$ as the unperturbed reference shock.

Figure 6 shows $n_i(x, y)$ and $B(x, y)$ at the time $t = 7000$, when the perturbed shocks in the three simulations have left the perturbation layer and entered the spatially uniform ambient plasma. Figures 6(a, c, e) show in each simulation j a localized peak of the ion density at $x \approx 22$. All shocks lag behind the reference shock. The shape of the density peak varies between the simulations. With respect to the upstream region, the shock front is concave near $y = 10$ in simulation 3 and follows the isocontour of the magnetic amplitude. It is almost planar at $y \approx 5$ in simulation 2 and convex at $y \approx 3$ in simulation 1. We also observe a structure with a reduced ion density, which is a signature of an ion phase space vortex like the ones shown in Fig. 4, at $x \approx 16$ and a non-planar front of the dense blast shell for $x \approx 14$.

Figures 6(b, d, f) show that the distributions of $B(x, y)$ react to the density modulations of the shock fronts. The varying density of mobile ions in the perturbation layer affected the balance between the thermal- and magnetic pressures downstream of the shock and the ram pressure of the upstream ions. The magnetic field expanded in the upstream direction in intervals with a low density of mobile ions. We observe bent magnetic field lines at the shock and around the ion phase space vortex. The curves $x_{c,j}(y) = 22.5 - A_j \sin(2\pi y/L_{y,j})$ with $A_j/L_{y,j} = 0.021$ follow the modulation of the front of $B(x, y)$. The supplementary movie 2 (simulation 1), movie 3 (simulation 2), and movie 4 (simulation 3) show the evolution of the shocks in the perturbation layer. It demonstrates that the density and magnetic field perturbations grow, saturate, and remain stationary until they leave it. This differs from what we observed in Fig. 5(a) where the distance between the reference shock and the perturbed shock steadily increased until the shock left the perturbation layer.

The density oscillation along y and around $x \approx 22$ in Fig. 6(a, c, e) induces an electric field that points from the dense to the dilute plasma and accelerates ions. It acts as a standing surface wave with a wavenumber $k_{y,j} = 2\pi/L_{y,j}$. Electrons can move freely along the magnetic field and the perturbation could thus oscillate in the ion-acoustic mode with the frequency $\omega_{cs,j} = c_s k_{y,j}$. If it does, it will oscillate with $\omega_{cs,1} \approx 0.36\omega_{lh}$, $\omega_{cs,2} = 0.24\omega_{lh}$, and $\omega_{cs,3} = 0.12\omega_{lh}$ in simulations 1 to 3. The density perturbation along y is also coupled to the shock with its average normal along x . The upstream plasma that crosses the shock is compressed by a FMS mode with a frequency close to ω_{lh} . The large difference between the ion-acoustic frequency and ω_{lh} allows us

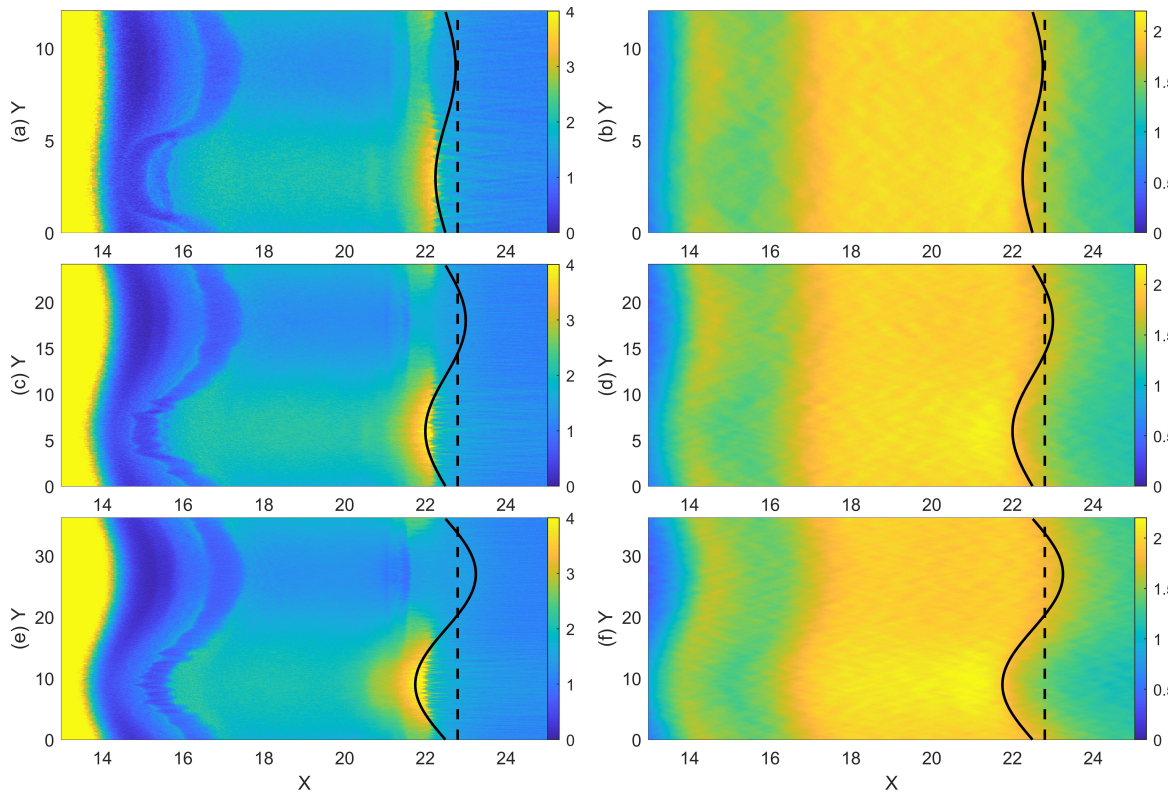


Figure 6. Ion density $n_i(x, y)$ and in-plane magnetic field amplitude $B(x, y)$ at $t = 7000$: Panels (a) and (b) show $n_i(x, y)$ and $B(x, y)$ computed by simulation 1 and panels (c) and (d) those of simulation 2. Panels (e) and (f) show the $n_i(x, y)$ and $B(x, y)$ computed by simulation 3. The dashed line denotes the average position of the unperturbed shock and the solid line corresponds to $x_c(y)$.

to distinguish between both.

For every data time step, we determine the maximum value of the ion density along x as a function of y , which gives us a density distribution $n_{i,max}(y, t)$. We also determine for each y the location where we reach $B(x, y) = 1.67$ first coming from the upstream region, which gives us the evolution in time of a curve $x_B(y, t)$ that is similar to the solid curve in Figs. 6(b, d, f). The imaginary part of the fundamental frequency of the Fourier transform over space of $x_B(y, t)$ and $n_{i,max}(y, t)$ gives us the amplitudes $x_B(k_{y,j}, t)$ and $n_{i,max}(k_{y,j}, t)$. Figure 7 plots $x_B(k_{y,j}, t)/L_{y,j}$ and $n_{i,max}(k_{y,j}, t)/L_{y,j}$. In simulation 1 $x_B(k_{y,j}, t)$ and $n_{i,max}(k_{y,j}, t)$ are strongly damped. Both curves reach extrema at around $t = 1.1 \times 10^4$ and converge to a steady state after that. Weaker damping in simulation 2 yields pronounced extrema at $t \approx 10^4$ and weaker ones at $t \approx 1.3 \times 10^4$. Both curves in simulation 3 oscillate in antiphase with the period ≈ 6000 . The oscillation frequency is lowest in simulation 1 and it is similar in simulations 2 and 3, which is not what we expect from ion-acoustic oscillations with $\omega_{cs,1} = 2\omega_{cs,2}$ and $\omega_{cs,1} = 3\omega_{cs,3}$. Simulation 3 gives us the oscillation frequency $0.75\omega_{lh}$ or $6.25\omega_{cs,3}$.

Lower-hybrid waves have been analyzed in uniformly magnetized plasma [46, 47]. They trap electrons magnetically and the trapped electrons confine the ions electrically.

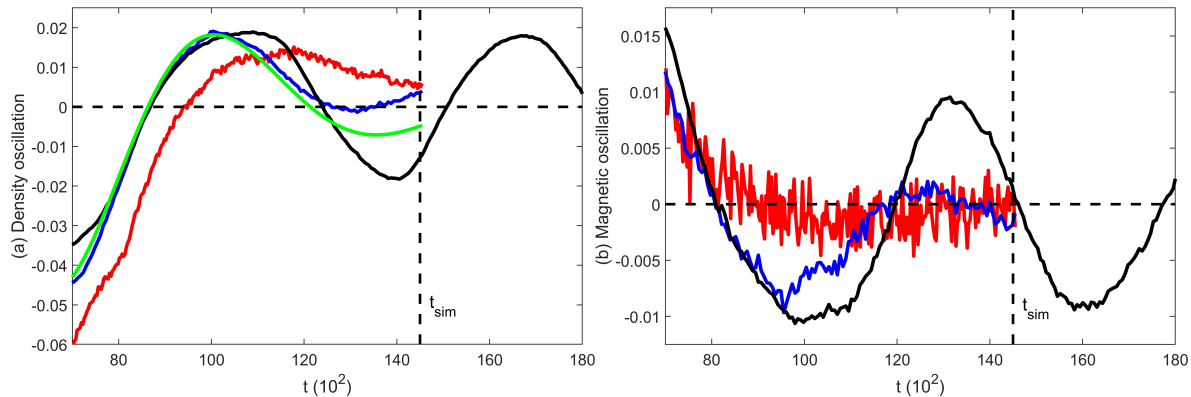


Figure 7. Oscillations of the ion peak density $n_{i,max}(k_{y,j},t)$ are plotted in panel (a) and the isocurves $x_B(k_{y,j},t) = 1.67$ of $B(x,y)$ are plotted in panel (b). The red curves correspond to simulation 1, the blue ones to simulation 2, and the black curves to simulation 3. The curve $C(t) = -0.044 \cdot \cos(\omega_f t - 0.2\pi) \cdot \exp(-0.3\omega_f t)$ with $\omega_f = 0.76\omega_{lh}$ is plotted in green in panel (a).

Lower-hybrid waves require that the trapped electrons do not move far along the magnetic field during $2\pi\omega_{lh}^{-1}$. Their wavevector, which is aligned with the density gradient, therefore has to be almost perpendicular to the magnetic field. The perturbation in our 2D simulation rotates the magnetic field direction and the density gradient differently and both will not remain mutually orthogonal. This rotation sets an upper limit on the amplitude of the spatial oscillations of the magnetic field and, hence, on the perturbation amplitude in our 2D simulations.

The angle θ between the wavevector of an undamped lower-hybrid mode and the magnetic field is limited to the range $|90^\circ - \theta| \lesssim \theta_{max}$. In a plasma with equal temperatures of electrons and ions, the angular range can be estimated with $\cos^2 \theta_{max} = m_e/m_i$, which yields $\theta_{max} \approx 0.4^\circ$ for nitrogen ions.

The perturbed shock propagates into an upstream plasma, which is spatially homogenous and does therefore not favor a specific propagation direction of the boundary oscillation. Hence, the surface wave and the mode that compresses the upstream plasma constitute a standing wave, which is composed of modes that propagate obliquely to the shock normal and in opposite directions. We can estimate the propagation angle θ_j of these modes relative to the background magnetic field as follows. According to the ion velocity distribution in the interval $37 \leq x \leq 41$ in Fig. 4(e), the wavelength of the lower-hybrid mode, which sustains the shock and forms the component of the wave that points along its normal, is $k_{x,s} \approx \pi$. The wavelength of the surface wave that moves along the shock boundary is $k_{y,j} = 2\pi/L_{y,j}$. The propagation angles $\theta_j = k_{x,s}/k_{y,j}$ are thus $\theta_1 = 80.5^\circ$, $\theta_2 = 85.2^\circ$, and $\theta_3 = 86.8^\circ$.

Shock modes do not have to be undamped as they are continuously fed with energy from the inflowing upstream plasma. The wave vector of the shock mode may however be rotated into a direction with less damping. Another aspect is that lower-hybrid waves with frequencies $\omega \approx \omega_{lh}$ and with $\theta = 90^\circ$ are dispersive [18]. If their phase

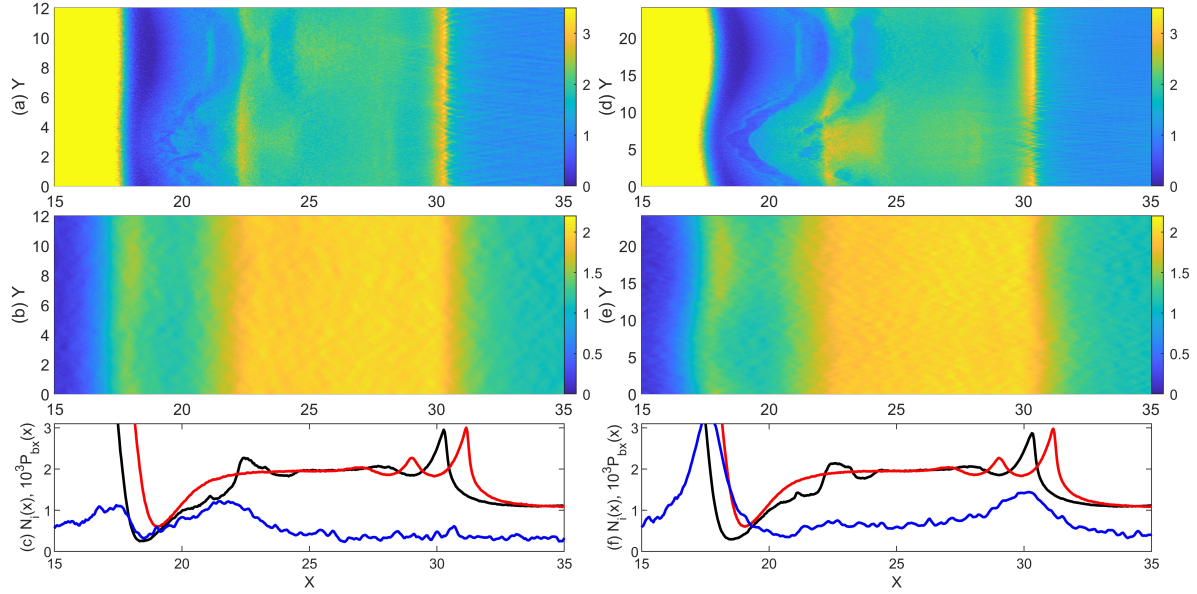


Figure 8. Distributions of the ion density $n_i(x, y)$ and the amplitude of the in-plane magnetic field $B(x, y)$ in simulations 1 (left column) and 2 (right column) at the time $t = 10^4$: Panels (a) and (d) show the ion density distributions. Panels (b) and (e) show $B(x, y)$. Panel (c) and (f) plot the box-averaged $N_i(x) = L_y^{-1} \int n_i(x, y) dy$ of the perturbed shock (black curve), of the reference shock (red curve), and the box-averaged magnetic pressure component $P_{bx} = L_y^{-1} \int (B_x(x, y)/B_0)^2 dy$ of the perturbed shock multiplied with 10^3 (blue curve).

velocity also changes with θ , we obtain an undamped surface wave only if the spread in wavenumbers along k_x and k_y is small. The higher resolution of k_y by simulation 3 allows the surface wave to involve wave modes with similar frequencies. Given that the shock fronts involve more than one wave mode, different spectral resolutions may also explain why their shapes differ in Figs. 6(a, c, e).

In addition to the requirement that lower-hybrid waves can only mediate a shock if they propagate almost perpendicularly to the background magnetic field, magnetic tension $(\mathbf{B} \cdot \nabla)\mathbf{B}/\mu_0$ is likely to contribute to the saturation of the perturbation. In simulation 3 and at the time depicted in Fig. 6(f), its magnitude is comparable to that of the magnetic pressure gradient force density $\nabla B^2/2\mu_0$ at $x \approx 22$ and $y \approx 9$ and about 20% of the thermal pressure gradient force density at the front of the shock in Fig. 6(e) at the same position (not shown). As we will see, the magnetic tension builds up over a much wider x -interval than the other forces and its impact on the saturation of the shock deformation in the perturbation layer is thus difficult to quantify.

3.2. Damping of the shock oscillations in simulation 1 and 2

We examine the distributions of the ion density and magnetic field amplitude at two times. Figure 8 shows them for simulations 1 and 2 at the time $t = 10^4$, when the curves for simulation 2 went through their extrema in Fig. 7. The perturbation of the shock

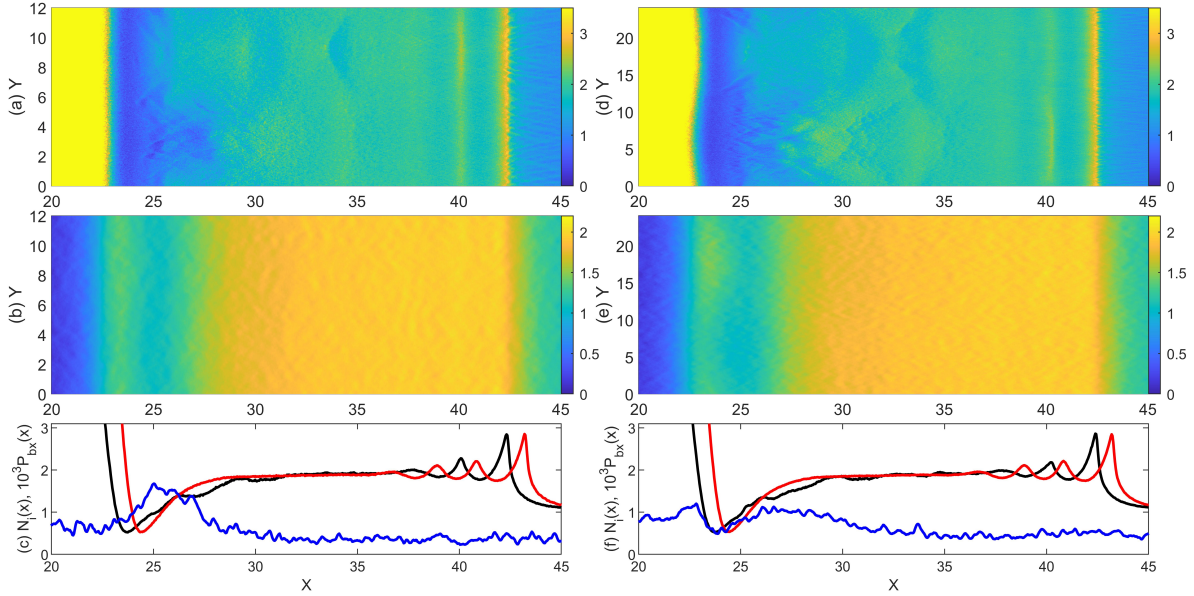


Figure 9. Distributions of the ion density $n_i(x, y)$ and the amplitude of the in-plane magnetic field $B(x, y)$ in simulations 1 (left column) and 2 (right column) at the time t_{sim} : Panels (a) and (d) show the ion density distributions $n_i(x, y)$. Panels (b) and (e) show $B(x, y)$. Panel (c) and (f) plot the box-averaged $N_i(x) = L_y^{-1} \int n_i(x, y) dy$ of the perturbed shock (black curve), of the reference shock (red curve), and the box-averaged magnetic pressure component $P_{bx} = L_y^{-1} \int (B_x(x, y)/B_0)^2 dy$ of the perturbed shock multiplied with 10^3 (blue curve).

front in simulation 1, which is shown in Figs. 8(a, b), has damped out. The front is planar and the density of the overshoot and the magnetic amplitude does not vary with y . The front is located one electron skin depth behind that of the reference shock and P_{bx} , which quantifies the deformation of the magnetic field in the simulation plane, is at noise levels. The perturbation of the shock front in simulation 2 has the opposite phase than the initial one in Fig. 6(c, d); it is oscillating. In simulation 2, P_{bx} evidences a deformation of the magnetic field, which results in magnetic tension, in an interval with the width 3 centered on the shock.

Figure 9 shows that at $t = t_{sim}$, the shock perturbation has also damped out in simulation 2. The density distribution of simulation 1 in Fig. 9(a) shows another density maximum at $x \approx 40$. Its separation from the leading density maximum at $x \approx 42$ reveals that the wavelength of the lower-hybrid mode, which mediates the shock, is 2 and $k_{x,s} = \pi$ as we observed in the 1D simulations. The magnetic field near the shocks in both simulations is aligned with y at this time. The lag between the perturbed and unperturbed shocks in Figs. 9(c, f) is unchanged compared to that in Figs. 8(c, f).

3.3. Weakly damped oscillations in simulation 3

Figure 10 shows the ion density and magnetic field distributions at the times $t = 1.1 \times 10^4$ and 1.66×10^4 , when the curves $n_i(k_{y,3}, t)$ and $x_B(k_{y,3}, t)$ go through extrema in Fig. 7.

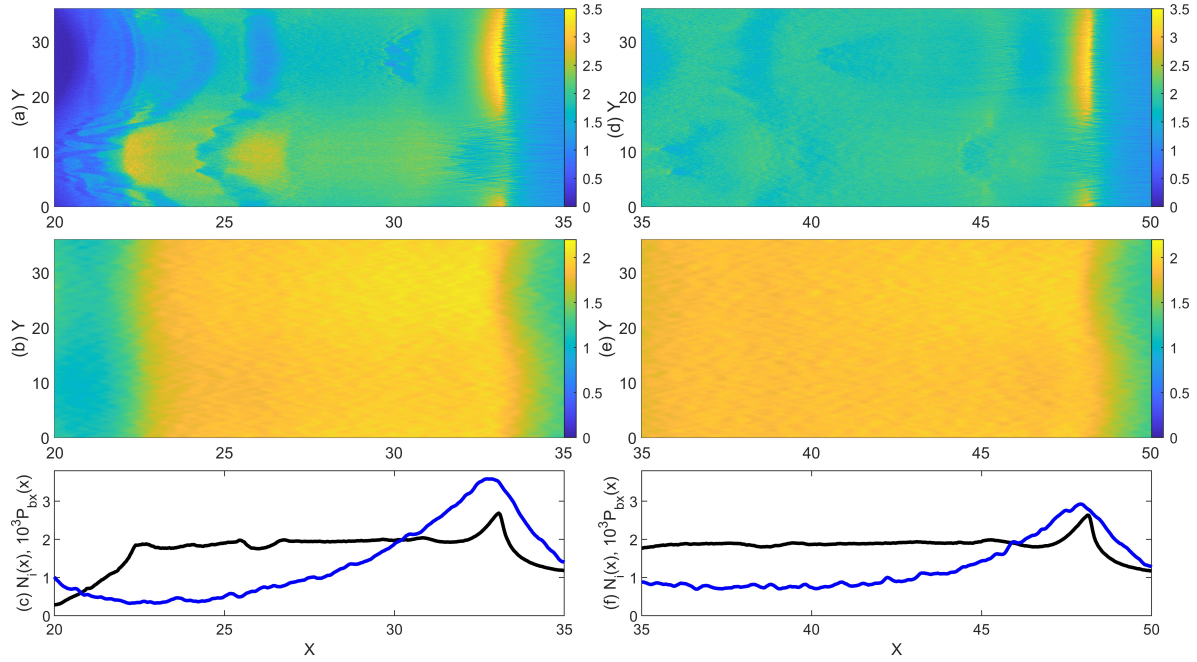


Figure 10. The plasma states at the times $t = 1.1 \times 10^4$ (left column) and 1.66×10^4 (right column) in simulation 3: Panels (a, d) show the ion density distributions $n_i(x, y)$. Panels (b, e) show the amplitude of the in-plane magnetic field $B(x, y)$. Panels (c) and (f) show the y -averaged ion density $N_i(x) = L_y^{-1} \int n_i(x, y) dy$ (black curves) and $P_{bx} = L_y^{-1} \int (B_x(x, y)/B_0)^2 dy$ (blue curves).

The oscillations of the shock fronts are in phase at the times $t = 1.1 \times 10^4$ and $t = 1.66 \times 10^4$ in simulation 3. Figure 10(a) reveals a density maximum at $x \approx 33$ and $y > 18$, which is concave with respect to the upstream region. A weak density enhancement near $y \approx 8$ bulges out into the upstream region. The position of the shock front is thus also a function of y and the variation is sinusoidal. The density oscillation is still present in Fig. 10(d). The front is almost flat, which indicates that some of the waves that sustained the shock have subsided. The in-plane magnetic field $B(x, y)$ in Figs. 10(b, e) is deformed near the shock front. It expands upstream in intervals, where the shock density is low. The supplementary movie 4 confirms that the shock front performs sinusoidal oscillations around its mean position along x , which are synchronized with those in the ion density along the shock front. The ion density oscillations are correlated with those of $B(x, y)$.

The curves in Fig. 10(c, f) show that the average ion density downstream of the shock is about 2; this shock does not compress the plasma much because the shock speed in the downstream frame is not small compared to the relative speed between the downstream and upstream plasma. According to P_{bx} , deformations of $B(x, y)$ are strongest near the shock front. They extend upstream and downstream and decrease exponentially with distance from the maximum. Note that the curve has its maximum behind the front because the strong magnetic field does not fill out the simulation box for all values of y at larger x . The peaks in the ion density have a much smaller spread

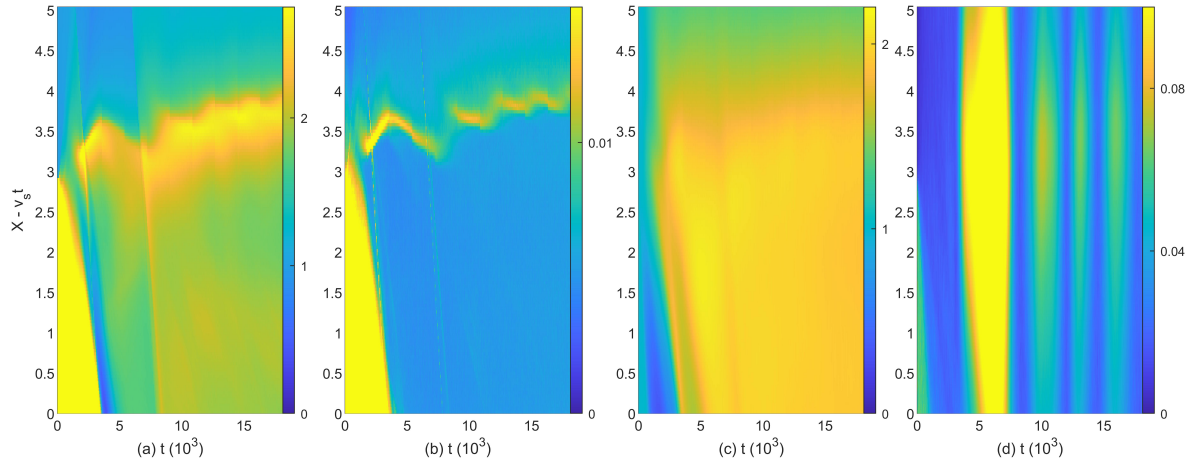


Figure 11. Y-averaged ion density and electromagnetic fields in a reference frame $\tilde{x} = x - v_s t$ that moves with $v_s = 1.6v_{fms}$. The shock is almost stationary in this reference frame. Panels (a) and (b) show the averaged ion density $N_i(\tilde{x}, t) = L_y^{-1} \int n_i(\tilde{x}, t) dy$ and the averaged amplitude modulus of the electric field in the simulation plane $\langle E^2 \rangle_y^{1/2}(\tilde{x}, t) = (e/L_{y,3} m_e c \omega_{pe}) (\int_y (E_x(\tilde{x}, t)^2 + E_y(\tilde{x}, t)^2) dy)^{1/2}$. Panels (c) and (d) show the average of the magnetic field modulus along y $\langle B_y^2 \rangle_y^{1/2}(\tilde{x}, t) = (\int_y (B_y(\tilde{x}, t)/B_0)^2 dy)^{1/2}$ and along x $\langle B_x^2 \rangle_y^{1/2}(\tilde{x}, t) = (\int_y (B_x(\tilde{x}, t)/B_0)^2 dy)^{1/2}$.

along x than their magnetic counterparts; charge density oscillations are shielded on Debye length scales and magnetic ones on skin depth scales.

Figure 11 shows the evolution in time of the y -averaged density and field distributions in simulation 3. We have transformed these distributions into a reference frame that moves with the speed $v_s = 1.6v_{fms}$ in the direction of the perturbed shock. Figure 11(a) shows that the shock is located at $\tilde{x} = x - v_s t \approx 3.5$. The position of its front oscillates in time. Its evolution is determined by a simultaneous oscillation of the shock front position, which varies with y and t , and of the density along the front. A strong in-plane electric field marks the front of the shock in Fig. 11(b) where the ion density gradient is largest. According to Fig. 11(c), the magnetic field is amplified by the shock crossing to more than twice its upstream value. The contribution of B_x to the magnetic pressure shown in Fig. 11(d) shows oscillations, which extend far into the upstream and downstream regions. The first and strongest maximum at early times is associated with the forced deformation of the shock as it propagated across the perturbation layer. After the shock left the perturbation layer, the shock performed free oscillations. They are coherent along the normal direction of the shock. Typical amplitudes of B_x are weak compared to B_y and we can thus interpret them as perturbations of an almost uniform guiding magnetic field that is aligned with y .

The supplementary movie 5 animates the ion phase space density distribution in time for the interval $x > 0$ and Fig. 12 shows its final frame. The shock reforms at the time $t \approx 1500$ and it remains stable after this time. It remains stationary in its comoving frame, which is typical for subcritical shocks. Some ions behind the shock are accelerated

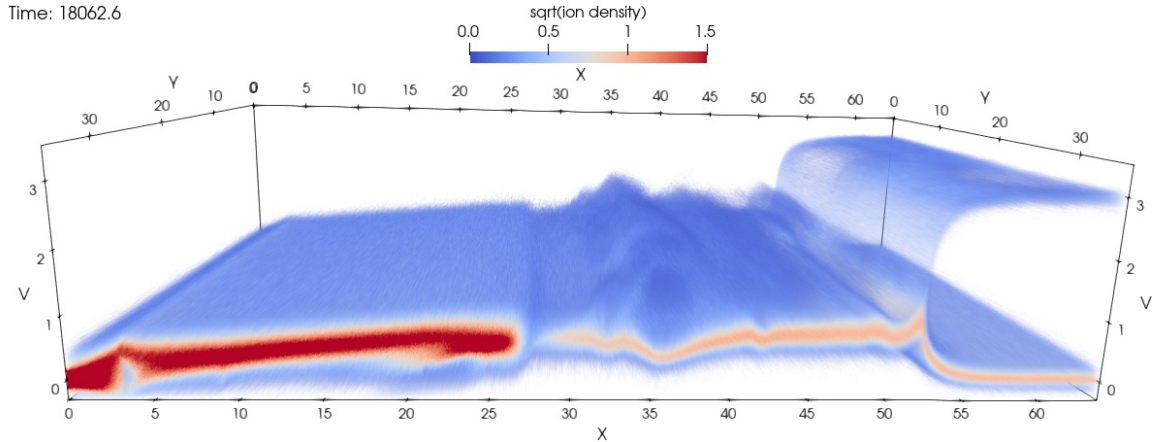


Figure 12. The square root of the ion phase space density at the time $t = 18000$ as a function of x , y , and $V = v_x/v_{fms}$. The density is normalized to the maximum phase space density of the ambient ions at the simulation's start and the color and opacity scales are linear.

to high energies forming phase space vortices with an axis that is approximately aligned with the y -axis. One such vortex survives at $x \approx 36$ in Fig. 12. A phase space vortex is sustained by the ambipolar electric field, which is associated with localized ion density depletion. The shock is located at $x \approx 53$ at this time and it accelerates a small fraction of the upstream ions to a speed $\approx 3v_{fms}$. The density of the shock-reflected ion beam is affected by the shock's density oscillation as can be seen from several patches with a reduced density. Since the upstream plasma outside of the perturbation layer has a uniform density, oscillations in the density of the shock-reflected ion beam must lead to a change in the number of ions that cross the shock and enter its downstream region.

4. Discussion

We studied with PIC simulations in one and two spatial dimensions the stability of shocks in collisionless plasma. A pair of shocks was driven by the thermal pressure jump between a thin, dense, and planar plasma cloud in the center of the simulation box, and a surrounding dilute ambient plasma. One shock propagated through a spatially uniform ambient plasma. The other shock traversed a perturbation layer, in which we varied the number density of mobile ions after it fully formed. We explored the reaction of subcritical fast magnetosonic (FMS) shocks to the perturbation.

In the 1D simulations, a lower density of mobile ions upstream of the shock increased the speed of its downstream plasma and reduced the shock speed in the downstream frame of reference. For our initial conditions, the net effect was that the shock was slowed down in intervals with a lower number density of mobile ions. It regained its initial speed once it left the perturbation layer. The spatial lag between the fastest and the slowest shock was about 2 electron skin depths, which was comparable to the wavelength of the wave that mediated the shock.

A variation in the density of the mobile ions in the perturbation layer along the shock front in the 2D simulations led to a spatial displacement of the shock front that was only a small fraction of the one we observed in the 1D PIC simulations. The amplitude of the spatial displacement was also proportional to the wavelength of the modulation; different parts of the shock front could thus not move independently. The crossing of the perturbation layer led to a modulation of the ion density of the shock front and to an expansion of the shocked magnetic field upstream. This expansion was more pronounced in regions with a low number density of mobile ions. Once a shock left the perturbation layer and entered the uniform plasma, the distributions of the ion density and position of the shock front, and the direction of the magnetic field changed.

We explored effects caused by the size of the simulation box along the shock front on the shock's evolution. The smallest box resolved a width of 12 electron skin depths, which is 6 times the wavelength of the wave that sustained the shock. The intermediate one doubled that width and the largest box tripled it. In the smallest simulation box, the shock perturbation damped out on a time scale less than an oscillation period of the mode that sustained the shock. In the intermediate simulation box, we observed a damped oscillation. Even weaker damping was observed in the largest box.

The frequency, with which the shock perturbation oscillated, was a large fraction of the lower-hybrid frequency. This frequency matches that of the FMS waves that mediated the shock in a simulation with similar initial conditions [18]. The ion density oscillations along the shock boundary and orthogonal to it constituted a standing wave, which is composed of modes that propagate in opposite directions and have a wavevector that is oblique to the shock normal. The limited thickness of the shock transition layer implies that the shock oscillation is not monochromatic. Fast magnetosonic waves close to their resonance frequency are known as lower-hybrid waves and they are dispersive. This means that their phase velocity changes with the wavevector. The damping of the shock may thus be caused by different frequencies of the lower-hybrid modes that constitute the shock. The larger the simulation box along the shock boundary, the better the shock is resolved in wavenumber space and the lower the frequency mismatch of the shock modes becomes. This may explain why the damping of the shock perturbation became weaker with the increasing size of the simulation box.

All simulations have shown that the shocks remain stable during their traversal of the perturbation layer and in the uniform plasma. The boundary oscillations are thus damped. We could, however, not track the shock long enough in the largest 2D simulation to determine its damping rate and, more specifically, if the amplitude decreases in time t with $t^{-3/2}$ as derived for some (magneto)hydrodynamic shocks. The boundary oscillations resulted in perturbations of the background magnetic field orthogonal to its direction. The background magnetic field was deformed in an interval that extended several electron skin depths upstream and downstream of the density overshoot of the shock in Figs. 10(c, f) and in Fig. 11(d). Such perturbations can trigger the growth of magnetowaves propagating in the Alfvén mode branch or in its high-frequency extension known as the Whistler wave branch [43], which extends up

to wave propagation angles that are almost perpendicular to the background magnetic field [48]. The damping of the shock boundary oscillations in the largest 2D simulation may be weak enough to lead to the growth of waves, which propagate along the background magnetic field. The box size and the simulation time we could resolve with our simulation were however not sufficiently large to resolve the Alfvén waves, which were observed in hybrid simulations [9], in PIC simulations with different initial and boundary conditions [12, 13, 17, 21], and by satellites [6].

We could also not determine unambiguously the mechanism, that lets the shock oscillation saturate in the 2D perturbation layer. The observation that lower-hybrid waves can only mediate a quasi-perpendicular shock and that the perturbation oscillates at the lower-hybrid frequency suggests that the amplitude of the shock boundary oscillation is limited by the stability properties of lower-hybrid waves. Another saturation mechanism could be magnetic tension, which was small compared to the thermal pressure gradient force but comparable in magnitude to the magnetic pressure gradient force. We leave these studies to future work.

It would be interesting to investigate shock oscillations in the laboratory. A wide range of shock studies in collisionless plasma exist but to the best of our knowledge, none has examined oscillations of the shock boundary. One caveat to such studies is that the wavelength of these oscillations is long and their amplitude small. We selected the magnetic field amplitude 0.85 T, the electron temperature 1000 keV and density 10^{15}cm^{-3} and fully ionized nitrogen ions, because these values are realistic for experiments, in which a laser-generated blast shell expands into an ambient plasma. An example is the shock formation study in Ref. [3]. However, a wavelength of the perturbation in simulation 3 would amount to 5 mm, which exceeds by far the spatial scales that was resolved by that study.

Acknowledgements

The simulations were performed on resources provided by the Swedish National Infrastructure for Computing (SNIC) at the NSC and on the centers of the Grand Equipement National de Calcul Intensif (GENCI) under grant number A0090406960. MED acknowledges financial support from a visiting fellowship of the Centre de Recherche Astrophysique de Lyon. AB and FCC acknowledge support by grant PID2021-125550OB-I00 from the Spanish Ministerio de Economía y Competitividad.

Data availability statement

All data that support the findings of this study are included within the article (and any supplementary files).

Conflict of interest

The authors declare that they have no conflict of interest.

References

- [1] Romagnani L, Bulanov S V, Borghesi M, Audebert P, Gauthier J C, Loewenbrueck K, Mackinnon A J, Patel P, Pretzler G, Toncian T and Willi O 2008 Observation of collisionless shocks in laser-plasma experiments *Phys. Rev. Lett.* **101** 025004
- [2] Kuramitsu Y, Sakawa Y, Morita T, Gregory C D, Waugh J N, Dono S, Aoki H, Tanji H, Koenig M, Woolsey N and Takabe H 2011 *Phys. Rev. Lett.* **106** 175002
- [3] Ahmed H, Dieckmann M E, Romagnani L, Doria D, Sarri G, Cerchez M, Ianni E, Kourakis I, Giesecke A L, Notley M, Prasad R, Quinn K, Willi O and Borghesi M 2013 Time-Resolved Characterization of the Formation of a Collisionless Shock *Phys. Rev. Lett.* **110** 205001
- [4] Schaeffer D B, Fox W, Habersberger D, Fiksel G, Bhattacharjee A, Barnak D H, Hu S X and Germaschewski K 2017 Generation and Evolution of High-Mach-Number Laser-Driven Magnetized Collisionless Shocks in the Laboratory *Phys. Rev. Lett.* **119** 025001
- [5] Fazzini A, Yao, W, Burdonov K, Béard J, Chen S N, Ciardi A, d'Humières E, Diab R, Filippov E D, Kisiov S, Lelasseux V, Miceli M, Moreno Q, Orlando S, Pikuz S, Ribeyre X, Starodubtsev M, Zemskov R, and Fuchs J 2022 Particle energization in colliding subcritical collisionless shocks investigated in the laboratory *Astron. Astrophys* **665** A87
- [6] Johlander A, Schwartz S J, Vaivads A, Khotyaintsev Yu V, Gingell I, Peng I B, Markidis S, Lindqvist P-A, Ergun R E, Marklund G T, Plaschke F, Magnes W, Strangeway R J, Russel C T, Wei H, Torbert R B, Paterson W R, Gershman D J, Dorelli J C, Avanov L A, Lavraud B, Saito Y, Giles B L, Pollock C J and Burch J L 2016 Rippled Quasiperpendicular Shock Observed by the Magnetospheric Multiscale Spacecraft *Phys. Rev. Lett.* **117** 165101
- [7] Winske D and Quest K B 1988 Magnetic field and density fluctuations at perpendicular supercritical collisionless shocks *J. Geophys. Res.* **93** 9681-9693
- [8] Lembege B and Savoini P 1992 Nonstationarity of a two-dimensional quasiperpendicular supercritical collisionless shock by self-reformation *Phys Fluids B* **4** 3533-3548
- [9] Lowe R E and Burgess D 2003 The properties and causes of rippling in quasi-perpendicular collisionless shock front *Ann. Geophys.* **21** 671
- [10] Chapman S C, Lee R E and Dendy R O 2005 Perpendicular shock reformation and ion acceleration *Space Sci. Rev.* **121** 5-19
- [11] Burgess D and Scholer M 2007 Shock front instability associated with reflected ions at the perpendicular shock *Phys. Plasmas* **14** 012108
- [12] Yang Z W, Lembege B and Lu Q M 2012 Impact of the rippling of a perpendicular shock front on ion dynamics *J Geophys Res* **117** A07222
- [13] Clark S E, Everson E T, Schaeffer D B, Bondarenko A S, Constantin C G, Niemann C and Winske D 2014 Enhanced collisionless shock formation in a magnetized plasma containing a density gradient *Phys. Rev. E* **90** 041101
- [14] Dieckmann M E, Sarri G, Doria D, Ahmed H and Borghesi M 2014 Evolution of slow electrostatic shock into a plasma shock mediated by electrostatic turbulence *New J. Phys.* **16** 073001
- [15] Burgess D, Hellinger P, Gingell I and Tavnicek P M 2016 Microstructure in two- and three-dimensional hybrid simulations of perpendicular collisionless shocks *J Plasma Phys* **82** 905820401
- [16] Marcowith A, Bret A, Bykov A, Dieckman M E, Drury L O, Lembege B, Lemoine M, Morlino G, Murphy G, Pelletier G, Plotnikov I, Reville B, Riquelme M, Sironi L and Novo A S 2016 The microphysics of collisionless shock waves *Rep. Prog. Phys.* **79** 046901
- [17] Umeda T and Daicho Y 2017 Periodic self-reformation of rippled perpendicular collisionless shocks in two dimensions *Ann Geophysicae* **36** 1047-1055

- [18] Dieckmann M E, Folini D, Walder R, Romagnani L, d’Humieres E, Bret A, Karlsson T and Ynnerman A 2017 Emergence of MHD structures in a collisionless PIC simulation plasma *Phys. Plasmas* **24** 094502
- [19] Gueroult R, Ohsawa Y and Fisch N J 2017 Role of Magnetosonic Solitons in Perpendicular Collisionless Shock Reformation *Phys. Rev. Lett.* **118** 125101
- [20] Dieckmann M E, Moreno Q, Doria D, Romagnani L, Sarri G, Folini D, Walder R, Bret A, d’Humieres E and Borghesi M 2018 Expansion of a radially symmetric blast shell into a uniformly magnetized plasma *Phys. Plasmas* **25** 052108
- [21] Kobzar O, Niemiec J, Amano T, Hoshino M, Matsukity S, Matsumoto Y and Pohl M 2021 Electron Acceleration at Rippled Low-mach-number Shocks in High-beta Collisionless Cosmic Plasmas *Astrophys J* **919** 97
- [22] Marshall W 1955 The structure of magneto-hydrodynamic shock waves *Proc. R. Soc. A* **233** 367
- [23] Edmiston J P and Kennel C F 1984 A parametric survey of the 1st critical Mach number for a fast MHD shock *J. Plasma Phys.* **32** 429-441
- [24] Gedalin M, Dimmock A P, Russel C T, Pogorelov N V and Roytershteyn V 2023 Role of the overshoot in the shock self-organization *J Plasma Phys* **89** 905890201
- [25] Cramer N F 1995 The theory of Alfvén surface waves *Phys. Scr.* **1995** 185
- [26] Joarder P S and Nakariakov V M 2006 Hydromagnetic surface waves on a tangential discontinuity *Geophys. Astrophys. Fluid Dyn.* **100** 59-83
- [27] Lysak R L 2008 On the dispersion relation for the kinetic Alfvén wave in an inhomogeneous plasma *Phys. Plasmas* **15** 062901
- [28] Forslund D W, Morse R L and Nielson C W 1970 Electron Cyclotron Drift Instability *Phys. Rev. Lett.* **25** 1266-1270
- [29] Davidson R C, Gladd N T, Wu C S and Huba J D 1977 Effects of finite plasma beta on the lower-hybrid-drift instability *Phys. Plasmas* **20** 301
- [30] Daughton W 2003 Electromagnetic properties of the lower-hybrid drift instability in a thin current sheet *Phys. Plasmas* **10** 3103-3119
- [31] McClements K G, Dendy R O, Bingham R, Kirk J G and Drury L O 1997 Acceleration of cosmic ray electrons by ion-excited waves at quasi-perpendicular shocks *Mon. Not. R. Astron. Soc.* **291** 241-249
- [32] Gekelman W, Vincena S, Van Compernelle B, Morales G J, Maggs J E, Pribyl P and Carter T A 2011 The many faces of shear Alfvén waves *Phys. Plasmas* **18** 055501
- [33] Roberts A E 1945 See National Technical Information Service Document PB2004-100597 [A. E. Roberts, Los Alamos Scientific Laboratory Report No. LA-299 1945 (unpublished)]. Copies may be ordered from National Technical Information Service, Springfield, VA 22161.
- [34] Freeman N C 1955 A theory of the stability of plane shock waves *Proc. R. Soc. Lond. A. Math. Phys. Sci.* **228** 341
- [35] Zaidel P M 1960 Shock wave from a slightly curved piston *J. Appl. Math. Mech.* **24** 316
- [36] D’yakov S P 1954 Shock wave stability *Zh. Eksp. Teor. Fiz.* **27** 288
- [37] Kontorovich V M 1957 On the shock waves stability *Zh. Eksp. Teor. Fiz.* **33** 1525
- [38] Wetta N, Pain J.-C, and Heuzé O 2018 D’yakov-Kontorovitch instability of shock waves in hot plasmas *Phys. Rev. E* **98**, 033205
- [39] Huete C, Cobos-Campos F, Abdikamalov E, and Bouquet S 2020 Acoustic stability of nonadiabatic high-energy-density shocks *Phys. Rev. Fluids* **5** 113403
- [40] Esirkepov T Z 2001 Exact charge conservation scheme for Particle-in-Cell simulation with an arbitrary form-factor *Comput. Phys. Commun.* **135** 144-153
- [41] Arber T D, Bennet K, Brady C S, Lawrence-Douglas A, Ramsay M G, Sircombe N J, Gillies P, Evans R G, Schmitz H, Bell A R and Ridgers C P 2015 Contemporary particle-in-cell approach to laser-plasma modelling *Plasma Phys. Control. Fusion* **57** 113001
- [42] Gardner C, and Krusal M 1964 Stability of plane magnetohydrodynamic shocks *Phys. Fluids* **7** 700

- [43] Graham D B, Khotyaintsev Yu V, Norgren A, Vaivads A, André M, Drake J F, Egedal J, Zhou M, Le Contel O, Webster J M, Lavraud B, Kacem V, Génot V, Jacquy C, Rager A C, Gershman D J, Burch J L, and Ergun R E 2019 Universality of Lower Hybrid Waves at Earth's Magnetopause *J. Geophys. Res.* **124**, 8727
- [44] Eliasson B and Shukla P K 2006 Formation and dynamics of coherent structures involving phase-space vortices in plasmas *Phys. Rep.* **422** 225-290
- [45] Dieckmann M E, Ynnerman A, Chapman S C, Rowlands G and Andersson N 2004 Simulating thermal noise *Phys. Scripta* **69** 456-460
- [46] Verdon A L, Cairns I H, Melrose D B and Robinson P A 2009 Properties of lower hybrid waves *IAU Symp.* **257** 569-573
- [47] Verdon A L, Cairns I H, Melrose D B and Robinson P A 2009 Warm electromagnetic lower hybrid wave dispersion relation *Phys. Plasmas* **16** 052105
- [48] Artemyev A, Agapitov O, Mourenas D, Krasnoselskikh V, Shastun V and Mozer F 2016 Oblique Whistler-Mode Waves in the Earth's Inner Magnetosphere: Energy Distribution, Origins, and Role in Radiation Belt Dynamics *Space Sci Rev* **200** 261-355